Layer-by-Layer Self-Assembly Composite Coatings for Improved Corrosion and Wear Resistance of Mg Alloy for Biomedical Applications

Tongfang Liu, Song Rui and Sheng Li *

College of Automotive Engineering, Hunan Mechanical & Electrical Polytechnic, Changsha 410151, China; nancy1210@163.com (T.L.); ss1010ss2021@163.com (S.R.)
* Correspondence: 173701007@csu.edu.cn

Abstract: Mg alloys are promising biomedical metal due to their natural degradability, good processability, and favorable mechanical properties. However, the poor corrosion resistance limits their further clinical applications. In this study, the combined strategies of surface chemical treatment and layer-by-layer self-assembly were used to prepare composite coatings on Mg alloys to improve the biocorrosion resistance. Specially, alkalized AZ91 Mg alloy generated chemical linkage with silane via Si–O–Mg covalent bond at the interface. Subsequently, Si–OH group from silane formed a crosslinked silane layer by Si–O–Si network. Further chemical assembly with graphene oxide (GO), lengthened the diffusion pathway of corrosive medium. The chemically assembled composite coatings could firmly bond to Mg alloy substrate, which persistently and effectively acted as compact barriers against corrosion propagation. Improved biocorrosion resistance of AZ91 Mg alloy with self-assembly composite coatings of silane/GO was subsequently confirmed by immersion tests. Besides, the Mg alloy exhibited good wear resistance due to outside layer of GO with a lubricant effect. Cell viability of higher than 75% had also been found for the alloy with self-assembly composite coatings, which showed good cytocompatibility.

Keywords: corrosion resistance; Mg alloy; wear resistance; biomedical applications

1. Introduction

Due to the merits of natural biodegradability, good processability and favorable mechanical properties etc., Mg alloys display promising biomedical applications in urinary stent, vascular stent, artificial joints, etc., [1–5]. It can reduce the permanent metallic implant risks of thrombosis, inflammatory responses, physical irritation, and inability to adapt to the changes and growth of defect sites [6–8]. Yet, Mg alloys have a very low anti-corrosion property, especially under the physiological environment of human body, in which Mg (standard electrode potential of -2.37 V vs. SHE) with high chemical activity acts as anode of galvanic corrosion [9–12]. Furthermore, the corrosion products with porous and loose structure on Mg alloy substrate cannot slow down the corrosion process [13]. The rapid corrosion results in the early loss of mechanical stability, thereby the structural failure of Mg alloys [14–17]. Hence, it is of importance to improve the corrosion resistance for its potential applications [18].

Surface treatment is one of the major strategies being extensively explored nowadays to enhance the corrosion resistance of alloys [19–21]. It usually includes anodizing, ion implantation, and chemical conversion layer, etc., which prevents corrosive medium from penetrating onto the substrate surface at the initial stage [22–24]. This meets the biodegradation requirements of biomedical applications that metals slowly corrode initially and completely dissolve after completing their functions [25–27]. Among the methods of surface treatment, silane treatment is proved to be greatly promising for isolating Mg alloy substrate from corrosive medium. Silane is hydrolyzed to generate silanol

group when it is in contact with water. This permits attachment to Mg alloy surface through chemical bonding, which constructively promotes interfacial adhesion [28–30]. Moreover, the remaining silanol group can undergo self-crosslinking, producing a compact layer on Mg alloy substrate. Yet, the layer was too thin to effectively hinder corrosive medium penetration [31,32]. Moreover, it may hydrolyze again and lose its protective effect. Additionally, the layer has no self-lubricating ability and is easy to be worn [33,34].

Graphene oxide (GO) sheet, as a two-dimensional (2D) ultrathin material, is known for favorable tribological properties [35–37]. It readily adsorbs on the lubricated surfaces, which brings about a very low coefficient of friction [35,38]. Moreover, GO has also been investigated to protect metals from corrosion by some researchers. For example, Saud et al. prepared GO layer on TiNb shape memory alloys to improve the corrosion resistance by microwave sintering [39]. They found that corrosion resistance was greatly enhanced (from 620.7 $\Omega \cdot cm^2$ to 1760.7 $\Omega \cdot cm^2$) after coating of GO. Raghupathy et al. also studied the effect of GO on corrosion behavior of Cu–GO composite coatings and concluded that addition of GO into Cu matrix generated a fine granular layer, which increased corrosion resistance [40]. Additionally, GO shows good biostability and biocompatibility for biological applications according to the reports of Zheng et al. [41]. It should be noted that GO possesses many functional groups on edges or surfaces, such as carboxyl, hydroxyl, etc., which opens a new window to graft onto silane to generate a reliable bioactive layer on Mg alloy, thereby effectively protecting the substrate against corrosion.

The purpose of this study is to investigate the possibility of silane/GO composite coatings on AZ91 Mg alloy and thereby to improve Mg alloy corrosion resistance for potential biomedical applications. In this work, the process of layer-by-layer self-assembly was used to prepare silane/GO composite coatings on AZ91 Mg alloy. The wear behavior and biocompatibility were also evaluated.

2. Materials and Methods

2.1. Materials

The used Mg alloy substrate was commercial AZ91, which was purchased from Dongguan Jiazhou metal materials Co., Ltd., (Dongguan, China). AZ91 Mg alloy was cut into cuboid with the dimension of 10 mm × 10 mm × 2 mm. Then it was polished using 1500 grit SiC paper, washed under ultrasonication and dried in hot air (represented by AZ91 in this study). Silane reagent (3-aminopropyltriethoxysilane, APTES) was obtained from Beijing Bailingwei Technology Co., Ltd., (Beijing, China). The as-received graphene oxide (GO) sheet was from Beijing Huarei Ruike Chemical Co., Ltd., (Beijing, China).
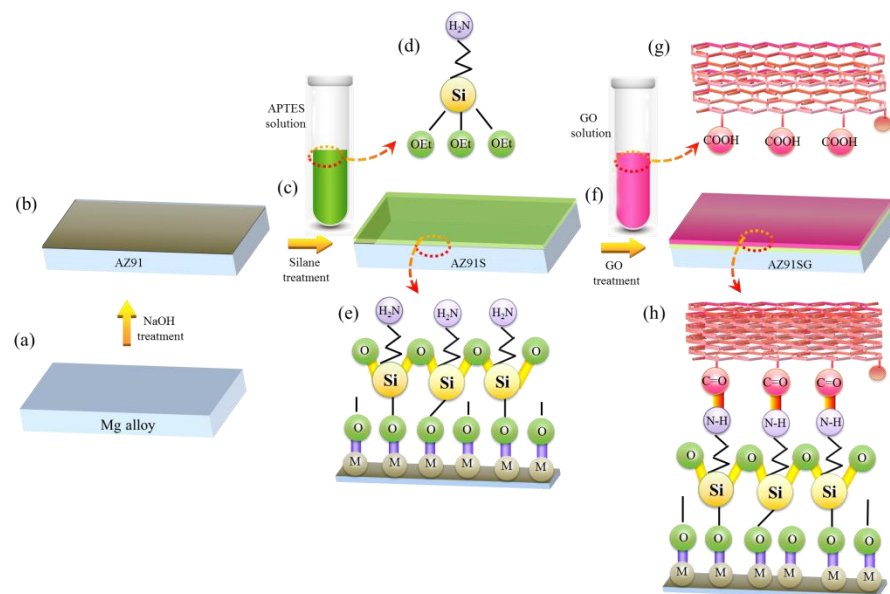
2.2. Substrate Treatment

2.2.1. Treatment with NaOH

To assemble silane on AZ91 Mg alloy, the substrate surface needed to carry a negative charge for chemical crosslinking. Treatment with NaOH would give rise to negatively charged surface because of the excess hydroxyl. Moreover, NaOH-treated Mg alloy surface produced an oxide layer with corrosion resistance. In this condition, NaOH treatment not only helped in the assembly of silane on Mg alloy substrate, but also formed an oxide layer against corrosion. The hydroxide-treated AZ91 Mg alloy substrate was illustrated in Figure 1a,b. The polished AZ91 Mg alloy substrate was first immersed in 4.5 M NaOH solution for 1.5 h at 35 °C, then thoroughly washed by deionized water and finally dried at 40 °C [42,43].

2.2.2. Treatment with Silane

To immobilize the GO sheet via chemical bonding, silane layer was prepared on the substrate. APTES (9 mL), water (11 mL), and ethanol (80 mL) were mixed together to prepare silane solution, which was under constant stirring for 1.5 h at room temperature to allow hydrolysis of APTES. AZ91 Mg alloy was functionalized chemically via immersing in hydrolyzed silane solution for 2.5 h in order to produce a linkage between Mg alloy

surface and silane group at the pH of 8.5 according to the literature [44], in which amino group was left for the next treatment with GO and silanol group was bonded onto Mg alloy substrate for a high linkage efficiency. The chemically functionalized AZ91 Mg alloy (denoted by AZ91S in Figure 1c–e) was first cleaned using distilled water to remove the irregular polymeric APTES and then dried at 35 °C in hot air for 65 min [43].

Figure 1. The schematic diagram of proposed layer-by-layer self-assembly lamellar structure between silane and GO sheets on AZ91 Mg alloy substrate. Treatment with (**a**,**b**) NaOH, (**c**–**e**) silane, (**f**–**h**) GO, respectively.

2.2.3. Treatment with GO

The as-received GO powder was dispersed in deionized water (115 mL) for 2.5 h under ultra-sonication to prepare suspension (1.3 mg/mL). GO suspension was used to treat AZ91S and the excessive GO sheets were removed by ultrasonication according to reports from Qi et al. [45]. AZ91S was first immersed into GO solution at 55 °C for 2.5 h, then removed out from GO solution and finally dried for 2.5 h at 55 °C [44,46]. These samples were denoted by AS31SG, as shown in Figure 1f–h.

2.3. Characterization of Layers

AZ91, AZ91S, and AZ91SG were examined by Nicolet 6700 Fourier transform infrared spectroscopy (FTIR; Nicolet iS50, Thermo Fisher Scientific, Waltham, MA, USA) with the method of reflection–absorption infrared reflectance. The spectrum data were obtained from 4000 cm^{-1} to 500 cm^{-1} with a resolution of 4 cm^{-1}. The surface morphologies of the layers on the samples were investigated by a scanning electron microscopy (SEM, Philips-XL30, Amsterdam, Netherlands) with an operating voltage of 5.0 kV. The compositions of layers on the samples were examined by energy-dispersive X-ray spectroscopy (EDS). An X-ray photoelectron spectroscope (XPS, ESCALAB 250, Thermo Fisher Scienticfic, Waltham, MA, USA) was used to examine the surface chemical compositions of the prepared layers on AZ91 Mg alloy substrate. The excitation source of XPS was Al Kα radiation and the binding energy of 284.8 eV (C1s, contaminated carbon) acted as reference value. The surface topography and roughness of samples were characterized by non-contact oscillating atomic force microscopy (AFM, LSM700, Zeiss, Braunschweig, Germany) to obtain surface information according to the method in the literature [47]. The tests were carried out at a scanning rate of 1 Hz with a resolution of 512 × 512 pixels at room temperature.

2.4. Biodegradation Tests

2.4.1. Immersion Tests

To check the stability of the silane-GO composite coatings on AZ91SG with AZ91 and AZ91S as control groups, immersion tests were performed using simulated body fluid (SBF). SBF contained of $K_2HPO_4 \cdot 3H_2O$ (0.231 g·L^{-1}), NaCl (8.035 g·L^{-1}), NaHCO$_3$ (0.355 g·L^{-1}), $MgCl_2 \cdot 6H_2O$ (0.311 g·L^{-1}), KCl (0.225 g·L^{-1}), Na$_2$SO$_4$ (0.072 g·L^{-1}), CaCl$_2$ (0.292 g·L^{-1}), $CH_2OH)_3CNH_2$ (6.118 g·L^{-1}). AZ91, AZ91S, and AZ91SG were soaked in SBF for 72 h. At the scheduled time during immersion process, the surface morphologies were observed by SEM and chemical compositions of the sample surfaces were analyzed by EDS.

2.4.2. H$_2$ Release, pH Changes, and Mg Ion Measurements

Based on the recommended method by Kirkland et al. [48], hydrogen release was measured via placing AZ91, AZ91S, and AZ91SG samples in SBF with the constant ratio of solution volume to surface area of 30:1 (mL/cm^2). The samples were suspended in an inverted funnel to allow for full surface exposure at 37 °C and the water level was measured according to a graduated burette. Three parallel samples for every condition were tested to determine the hydrogen evolution. The pH values of SBF were determined by over different immersion periods (24 h, 72 h, respectively) using a pH meter. The released Mg ions after immersion in SBF for 24 h and 72 h were measured by ICP-OES (inductively coupled plasma optical emission spectrometer, Agilent Technologies, Munich, Germany).

2.5. Wear Tests

The wear behaviors of AZ91SG with AZ91 as a control group were tested by a multifunctional material surface performance tester (CFT-I, Lanzhou Zhongke Kaihua Technology Development Co. Ltd., Lanzhou, China), which was ball-on-disk. The test was under dry sliding friction condition according to the guidelines and the steel ball (hardness of 760–840 HV) with 4 mm in diameter moved in a linear (5 mm) at room temperature. The used load was 1.0 N and the test time was 30 min. The wear scar morphologies of AZ91SG with AZ91 as a control group were observed by optical interferometer (BX60, Olympus Corporation, Tokyo, Japan), respectively. Moreover, the corresponding 3D surface profilometer (ST400, Nanovea, Irvine, CA, USA) was used to characterize the wear area contour.

2.6. Cytocompatibility

The MTT (3-(4,5-dimethylthiazol-2-yl)-2,5-diphenyltetrazolium bromide) assay was performed to determine the cytocompatibility of AZ91SG for potential biomedical applications [49,50]. AZ91SG was initially sterilized for 30 min using UV radiation, then placed in DMEM (Dulbecco's modified Eagle's medium) for 72 h at 37 °C under humidified atmosphere (5% CO$_2$). The DMEM medium/surface area ratio was 1.25 mL/cm^2. The extracts of AZ91SG were centrifuged and stored for use at 4 °C. The MG-63 cell (human bone osteosarcoma cell) was used for the experiments. The cells (10^4 cells per mL) were incubated for 1 day. Subsequently, different dilutions of extracts (50% and 100%) were used as culture medium. The DMEM (0% of AZ91SG extract) was used as control group. After culture for 72 h, MTT dye was immitted to culture plate. Then DMSO (Dimethylsulfoxide) (100 mL per well) was used to dissolve the precipitated formazan. Finally, the absorbance was measured by a micro-plate reader (Hercules, CA, USA) at 450 nm and the cell viability was determined using the following equation [51]:

$$\text{Cell viability (\%)} = \text{absorbance}_{test}/\text{absorbance}_{control} \times 100\% \tag{1}$$

2.7. Statistical Analysis

All of the tests were carried out at least three times. Results were recorded as mean ±standard deviation. The difference between the groups was analyzed by one-way analysis of variance. * $p < 0.05$ was considered to be statistically different.

3. Results and Discussion

3.1. Surface Characteristics

The FTIR spectra for AZ91, AZ91S, and AZ91SG were shown in Figure 2. Apparently, all the FTIR spectra were quite different. It was clearly seen that no obvious peaks were observed for AZ91 metal substrate. In contrast, various distinct peaks occurred in FTIR spectrum for the case of AZ91S. An obvious doublet around 2980 and 2850 cm^{-1} was assigned to asymmetric and symmetric vibrations of methylene group (CH_2), indicating the successful combination of silane onto AZ91 Mg alloy substrate. Moreover, the chemical incorporation of silane was further confirmed by the appearance of a new peak at 1570 cm^{-1} as a result of the vibrational mode of amine group [52]. The Si–O–Si stretching vibration from AZ91S could be obviously observed around 1101 cm^{-1} [43,53], which indicated the formation of siloxane network among Si–OH group. The peak around 1043 cm^{-1} was assigned to the stretching in Si–O–Mg, which indicated the tight anchorage of silane on AZ91 substrate. Both Si–O–Mg and Si–O–Si bonds promoted the condensation of silane at the surface. Additionally, AZ91S did not exhibit a peak around 3690 cm^{-1}, indicating no hydroxyl groups in the sample, which was as a result of chemical reaction between magnesium hydroxyl and the silanol group from the hydrolyzed APTES. For AZ91SG, it could be found that there existed a broad hydroxyl (–OH) peak around 3600–3200 cm^{-1} after GO treatment [54]. Meanwhile, the transmittance peaks at 1630 cm^{-1}, 1401 cm^{-1}, and 1030 cm^{-1} corresponded to C=C, –C–OH and C–O–C, respectively, which accorded with the main absorption band of GO [55]. This indicated that GO has been successfully bonded onto AZ91S. It was noteworthy that the peak at 1670 cm^{-1} of the AZ91SG revealed the existence of –NH–C=O bond [56], implying the GO was grafted via amidation reaction between the carboxyl and amide groups. The incorporation of GO further increased the physical barriers against corrosion medium, which may effectively block the corrosion penetration and provide constructive protection for AZ91 substrate.
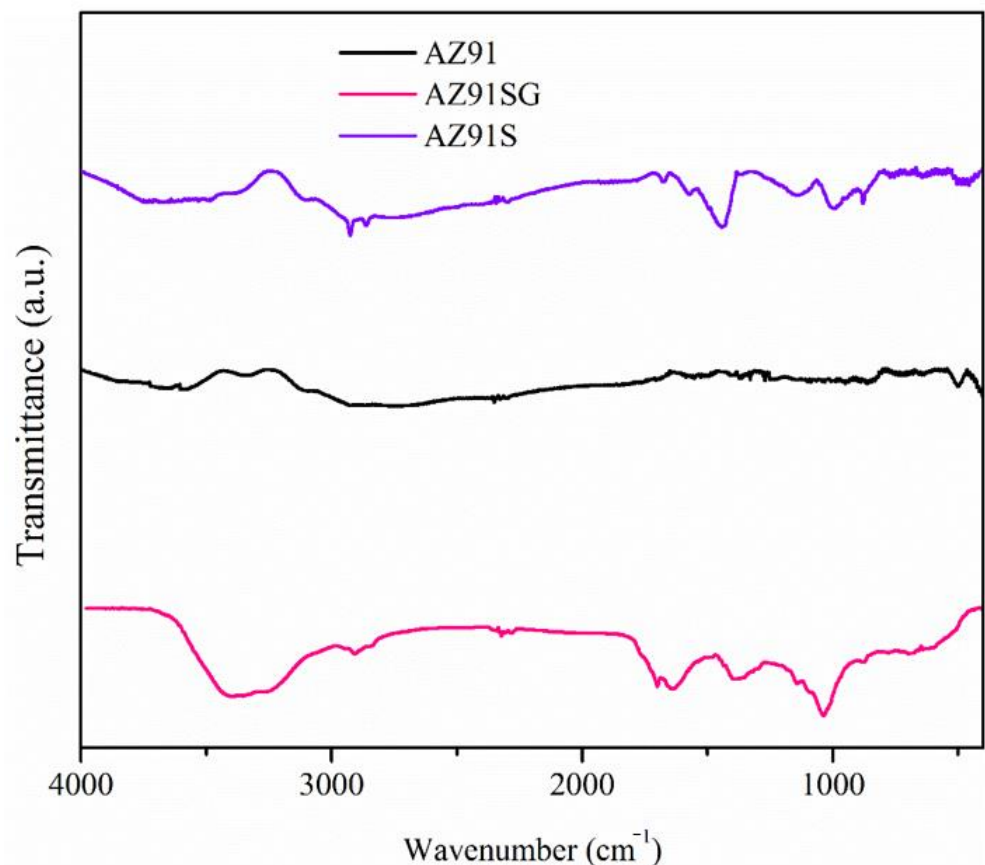

Figure 2. FTIR spectra for AZ91SG with AZ91 and AZ91S as the control groups.

The chemical compositions of AZ91S and AZ91SG were further analyzed by XPS to investigate the elements and valence states, as displayed in Figure 3a,d. The survey scan of AZ91S in Figure 3a showed the appearance of Si 2p, O 1s, N 1s, and C 1s peaks, etc., which confirmed the incorporation of silane on AZ91 Mg alloy. It could be concluded that Si 2p and N 1s peaks originated from silane, indicating that the covalent incorporation into AZ91 substrate occurred successfully. The Si 2p spectrum was shown in Figure 3b and it was deconvolved into two peaks: Si–O–Si (101.8 eV) and Si–O–Mg (102.4 eV) [43,57,58]. The formation of Si–O–Si indicated the cross-link network of silane. The Si–O–Mg was assigned to the reaction between silanol from hydrolyzed silane and alkalined AZ91 Mg alloy. As displayed in Figure 3c, the survey scan of AZ91SG showed the appearance of O 1s, N 1s, and C 1s peaks. Moreover, high-resolution spectrum of C 1s was presented in Figure 3d. The C 1s peak could be fitted at 284.7 eV, 285.3 eV, and 288.5 eV using Gaussian–Lorentzian curve, which were typically for C–C/C=C, C–OH and C–C=O groups, respectively, which implied that GO was bonded to AZ91S. The reuslt was consistent with the results in the literature [43,59,60].
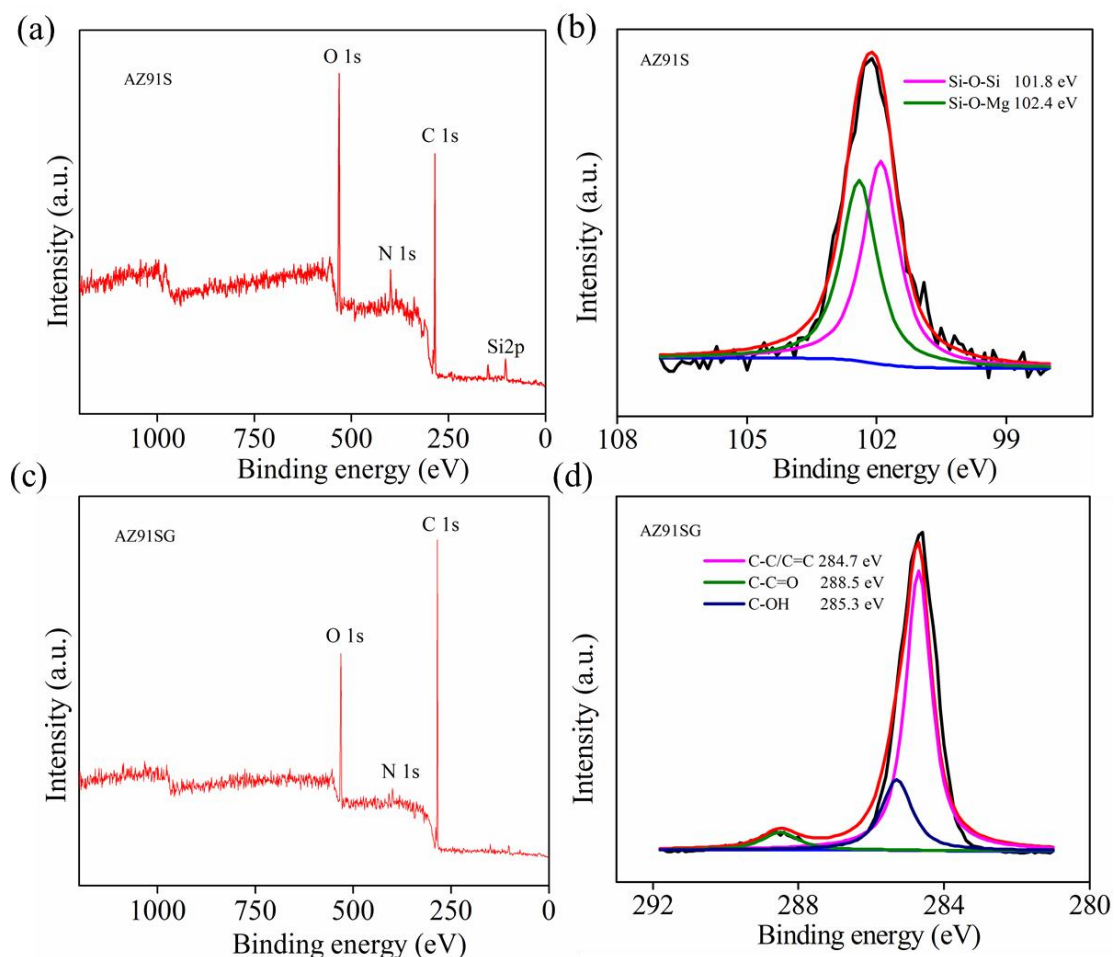
Figure 3. Survey XPS spectra of (**a**) AZ91S with high resolution of (**b**) Si 2p spectrum; Survey XPS spectra of (**c**) AZ91SG with high resolution of (**d**) C 1s spectrum to further study the chemical interaction between silane and GO.

The AFM topographic images of AZ91, AZ91S, and AZ91SG were used to evaluate the surface characteristic because of the interactions of silane or/and GO layers on metal substrate. The AFM images showed an obvious difference among them. It could be found that on the surface of AZ91 there appeared some scratches or grooves in Figure 4a. Waviness of the profile along the red plane had become pronounced, as shown in Figure 4b. Profile roughness value (*Pa*) and areal roughness value (*PSa*) for AZ91 in Figure 4c were

17.2 and 18.9 µm respectively, which was caused by grinding. When silane was bonded onto Mg alloy substrate, the surface of AZ91S was still scratched, but the scratches in Figure 4d were slightly covered, as demonstrated by waviness of the profile in Figure 4e. The *Pa* and *PSa* slightly decreased to 15.1 and 11.1 µm in Figure 4f, respectively. These results indicated that the treatment with silane changed the surface morphologies of AZ91, resulting in relatively even and smooth surface on AZ91S. The treatment with GO on AZ91S further changed the surface morphologies. Uneven surface morphology of AZ91SG was observed in Figure 4g, which was clearly different from that of AZ91S. The *Pa* and *PSa* increased to 19.1 and 20.2 nm in Figure 4i, respectively. This phenomenon might result from the full coverage of Go with wrinkles on the surface [53].
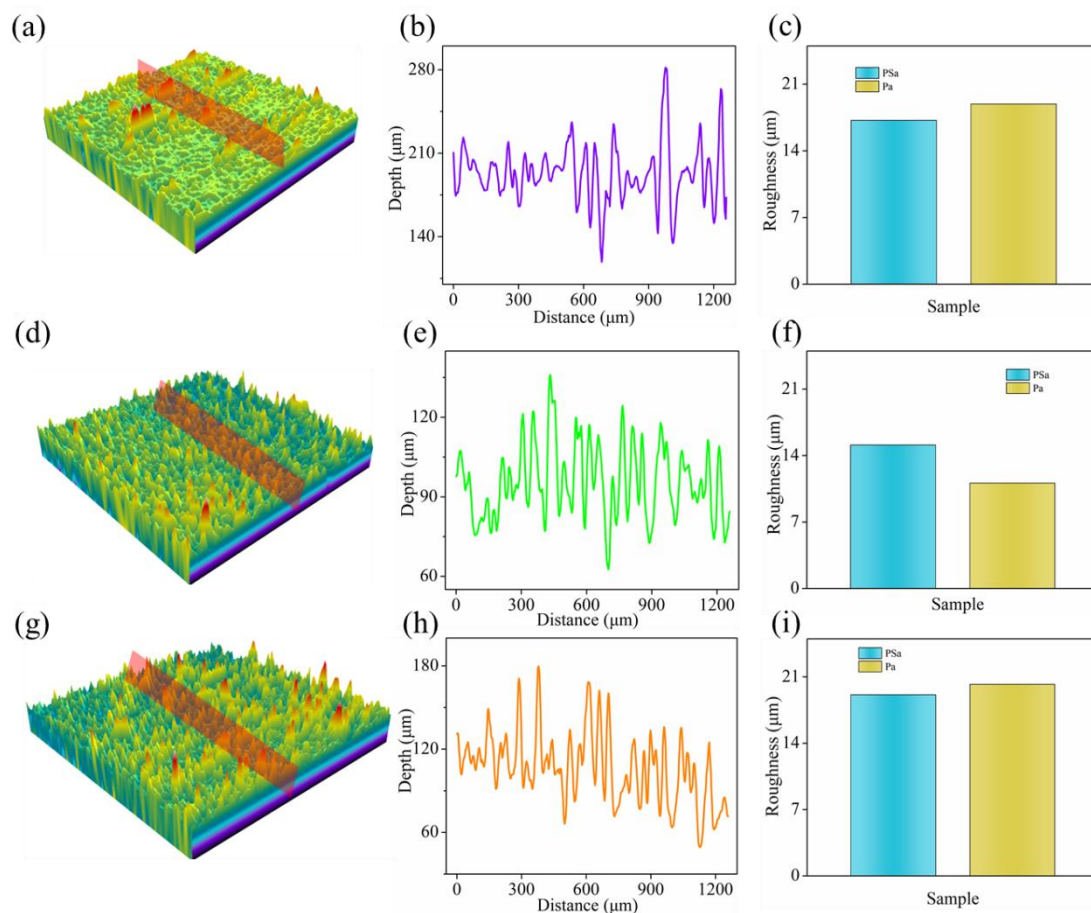

Figure 4. Representative AFM images of (**a**) AZ91, (**d**) AZ91S and (**g**) AZ91SG; Height profile along the red plane of (**b**) AZ91, (**e**) AZ91S and (**h**) AZ91SG with corresponding roughness for (**c**) AZ91, (**f**) AZ91S, (**i**) AZ91SG.

3.2. Corrosion Performance

The surface morphologies of AZ91, AZ91S, and AZ91SG were examined using SEM in conjunction with EDS to study the surface stability and the distribution of elements after immersion tests. The time-dependent surface morphologies are shown in Figure 5. It was clear that the entire surface of AZ91 in Figure 5a was covered with corrosion products with oval or round appearance. After immersion for 72 h, the corrosion on AZ91 surface was well localized, expressed by cavern and cracks in Figure 5b. The main elements of corrosion products on AZ91 were O and Mg, indicating the surface was severely corroded, as evidenced by EDS analysis of point A. Compared with AZ91, AZ91S exhibits a slightly mild condition. It could be found that corrosion attack mostly occurred through pitting with a small amount of corrosion products after immersion for 24 h in Figure 5c. The SEM images in Figure 5d showed that the bright corrosion products increased with increase in

immersion time for 72 h. Moreover, the corrosion products became larger. Based on EDS analysis of the large gray particles in Figure 5d as follows, the main chemical compositions were O, C, Mg, Ca elements. This was due to the formation of MgO, Mg(OH)$_2$, MgCO$_3$, CaCO$_3$, etc., in SBF according to the related reports by Liu, Gonzalez, et al. [61,62]. The corrosion for AZ91S might be related to the gradual hydrolysis or the ultrathin layer of silane. Corrosive medium led to the deterioration of the anti-corrosion property of AZ91S. As to AZ91SG, it exhibited a relatively dense and smooth surface with only a few bright corrosion products in Figure 5e,f after immersion for 24 h and even 72 h, indicating that the silane/GO composite coatings were stable and not changed much even on immersion in the SBF. The elemental mapping analysis of AZ91SG after immersion for 72 h was performed to assess the distributions of major components. The EDS elemental analysis showed that it had higher contents of C and Mg elements due to the presence of silane/GO composite coating with good protection effects on Mg alloy against corrosion. Element mapping in Figure 5g, especially C and O, proved the uniform distributions of silane/GO coatings. This offered reliable and long-term resistance against corrosion for Mg alloy substrate.
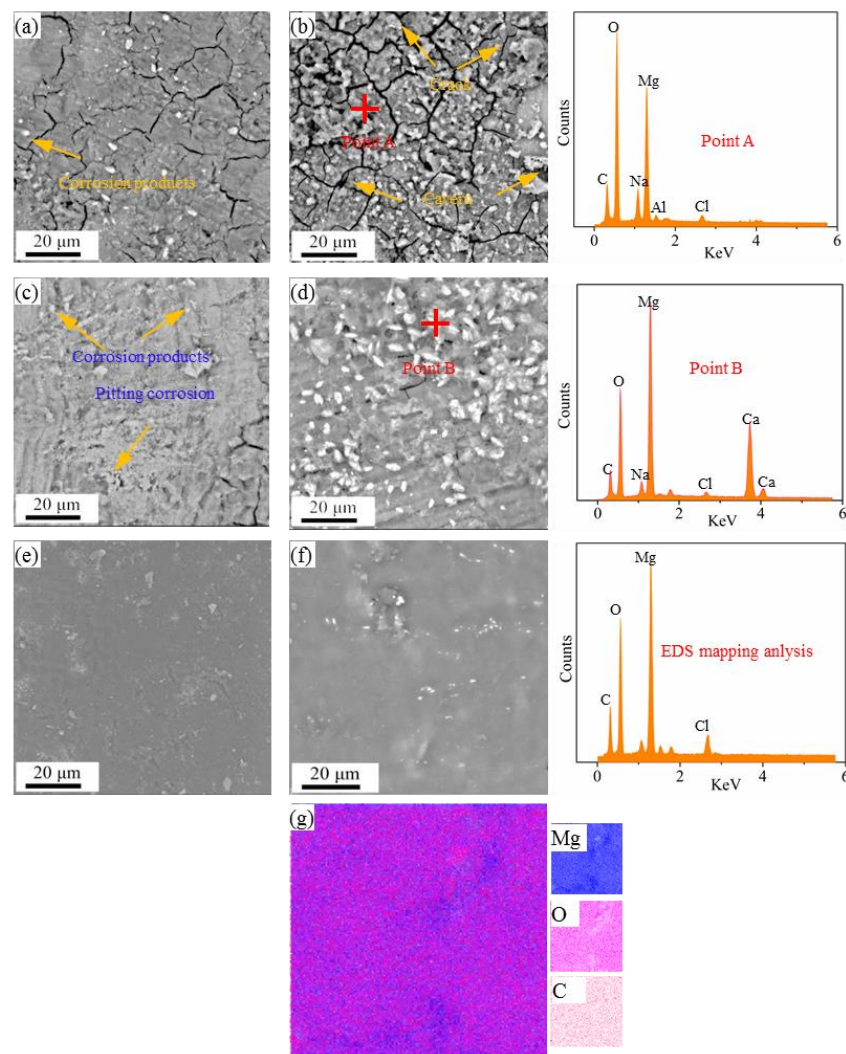
Figure 5. SEM in conjunction with EDS was used to study the surface morphologies and the distributions of elements during immersion tests: SEM images with EDS analysis of (**a**) AZ91, (**c**) AZ91S, and (**e**) AZ91SG after immersion for 24 h; (**b**) AZ91, (**d**) AZ91S, and (**f**) AZ91SG after immersion for 72 h, respectively. (**g**) United Mg O, and C element distributions on AZ91SG after immersion for 72 h.

AZ91SG possessed the best corrosion resistance, although it showed the largest surface roughness according to the AFM images in Figure 4i, suggesting that the roughness was not the dominant factor for corrosion attack in this study. This might be related to the dense and compact structure of silane/GO composite coatings on Mg alloy substrate. Gu [63] also reported that NaHCO$_3$-treated Mg–Ca alloy with large surface roughness showed high corrosion resistance and presented an extremely reduced corrosion process.

Mg ion concentration was utilized to assess the anti-corrosion effects of silane/GO composite coatings on AZ91 Mg alloy, and the released Mg ions in the SBF were analyzed by ICP-OES, as exhibited in Figure 6a. For AZ91, the released Mg ion up to 72 h increased from 1.44 mM/cm^2 (24 h) to 4.32 mM/cm^2. In contrast, AZ91SG showed a very slow release of Mg ion ranging from 0.12 mM/cm^2 (24 h) to 0.34 mM/cm^2 (72 h), which was 0.544 g/L. It could be observed that the average release rate of Mg ion for AZ91SG was much lower than that of AZ91 during 72 h of immersion tests. The results clearly indicated that the corrosion of AZ91SG was markedly alleviated in comparison with AZ91. Furthermore, pH changes of SBF containing AZ91 and AZ91SG were shown in Figure 6b. Obviously, both pH values of samples were observed in the alkaline region. Moreover, the pH gradually increased with the prolongation of immersion time, especially for AZ91. It should be noted that AZ91SG was less alkaline in comparation with AZ91. This most possibly could be due to the protection of silane/GO composite coatings, as discussed in the immersion performance tests.
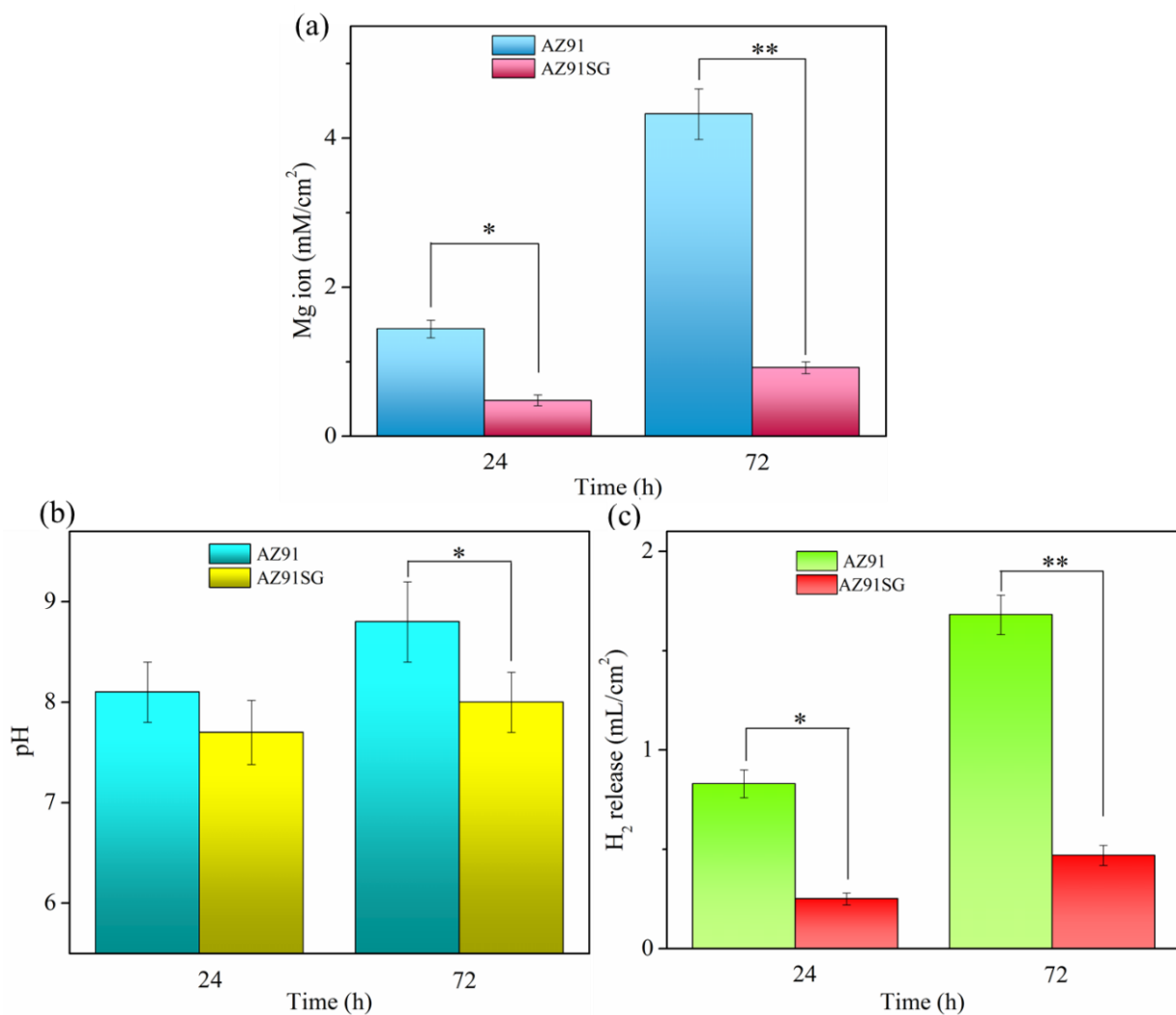

Figure 6. (**a**) Released Mg ions from ICP-OES measurement, (**b**) pH changes and (**c**) rates of H$_2$ release from AZ91SG with AZ91 as a control group over a period of 24 and 72 h, respectively.

Mg alloy surface layer might become unstable because of the released H_2. This not only corroded the underlying Mg alloy substrate, but also increased the electrolyte permeability through surface layer, thereby accelerating corrosion. In this study, H_2 release tests in SBF were performed on AZ91SG along with AZ91. The results were exhibited in Figure 6c. As expected, AZ91 showed a quick and copious release of H_2 with time, the H_2 release rate slightly decreased over immersion time. In contrast, AZ91SG only showed small amount of H_2 at the beginning of immersion tests, with less H_2 accumulation being found two days later. The trend in H_2 release was in agreement with that observed for pH and Mg ion release tested by ICP-OES.
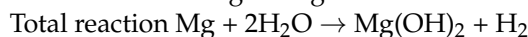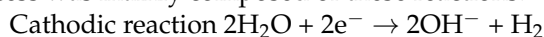
3.3. Wear Resistance

Wear behaviors of AZ91SG in comparison with AZ91 were displayed with the aid of optical morphologies, 3D interferograms. Optical morphologies of wear tracks provided an overview of the extent of damages. As shown in Figure 7a for AZ91, it could be observed that lots of grooves and ridges on the wear track were parallel to the sliding direction, which belonged to the abrasive wear behavior. Moreover, there were many wear marks and debris on worn interface zone, which suggested severe abrasion. Compared with AZ91, the amount of grooves and ridges on the wear track of AZ91SG decreased in Figure 7b. The wear damage was reduced with relatively less marks and debris on worn interface zone, suggesting that silane/GO composite coatings enhanced anti-wear resistance of Mg alloy. Moreover, 3D interferograms which related with wear track profile were shown in Figure 7c,d, respectively. For the wear track of AZ91, the maximum depth was 83 μm, and there were some protrusions. The surface showed different colors, indicating a server wear behavior. In contrast, for the wear track of AZ91SG, the maximum depth was only 52 μm, and the surface showed the relatively same color, representing a good protection capability of silane/GO composite coatings on Mg alloy substrate. The volume loss was evaluated according to three 3D interferograms with wear track profile in different wear areas [64,65]. Volume loss was calculated by length, width and height. In this way, the volume loss for AZ91 SG was approximately 0.31 times of that for AZ91.
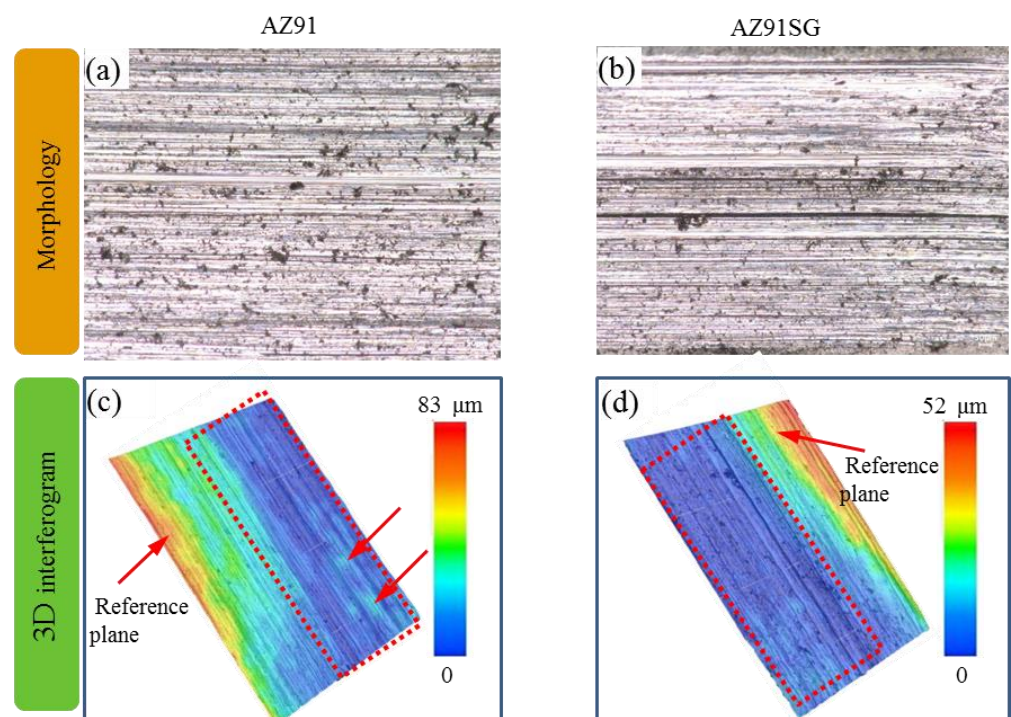

Figure 7. Optical images of wear tracks, 3D interferograms showing wear track profile for (**a**,**c**) AZ91 and (**b**,**d**) AZ91SG, respectively.

### 3.4. Protective Mechanism and Biomedical Applications

Mg alloys with high specific strength, low density, and good biocompatibility etc., represented a promising biomaterial for biomedical applications, such as urinary stent, vascular stent, etc. Compared with the currently used titanium-based biomedical metals, the major advantages of Mg alloys were low biocorrosion resistance. The biocorrrosion process was mainly composed of these reactions.

Cathodic reaction $2H_2O + 2e^- \rightarrow 2OH^- + H_2$

Anodic reaction $Mg \rightarrow Mg^{2+} + 2e^-$

Total reaction $Mg + 2H_2O \rightarrow Mg(OH)_2 + H_2$

However, the biodegradation process was too fast to meet the needs of biomedical metals due to the high chemical activity of Mg, especially in the environment containing chloride ion in SBF, which resulted in a further corrosion reaction:

$Mg(OH)_2 + 2Cl^- \rightarrow MgCl_2 + 2OH^-$
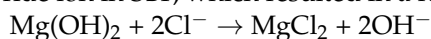
Surface treatment was an effective strategy to enhance the corrosion resistance. After treatment with NaOH, there exists an oxide layer against corrosion. Further treatment with silane, Si–O–Mg bond with high-density formed at the interface of alkalined AZ91 Mg alloy. Moreover, Si–O–Si network among Si–OH group formed. Both Si–O–Mg and Si–O–Si bonds promote a solid and condensation intermediate layer of silane. The silane layer acted a barrier to hinder electrolyte penetration, especially H_2O and Cl^-, thereby protecting underlying Mg alloy against corrosion. Furthermore, silane could chemically bond into GO through amidation reaction between amino and carboxyl groups [43], further lengthening and hindering the diffusion pathway of corrosive medium onto underlying Mg alloy surface, as shown in Figure 8a.
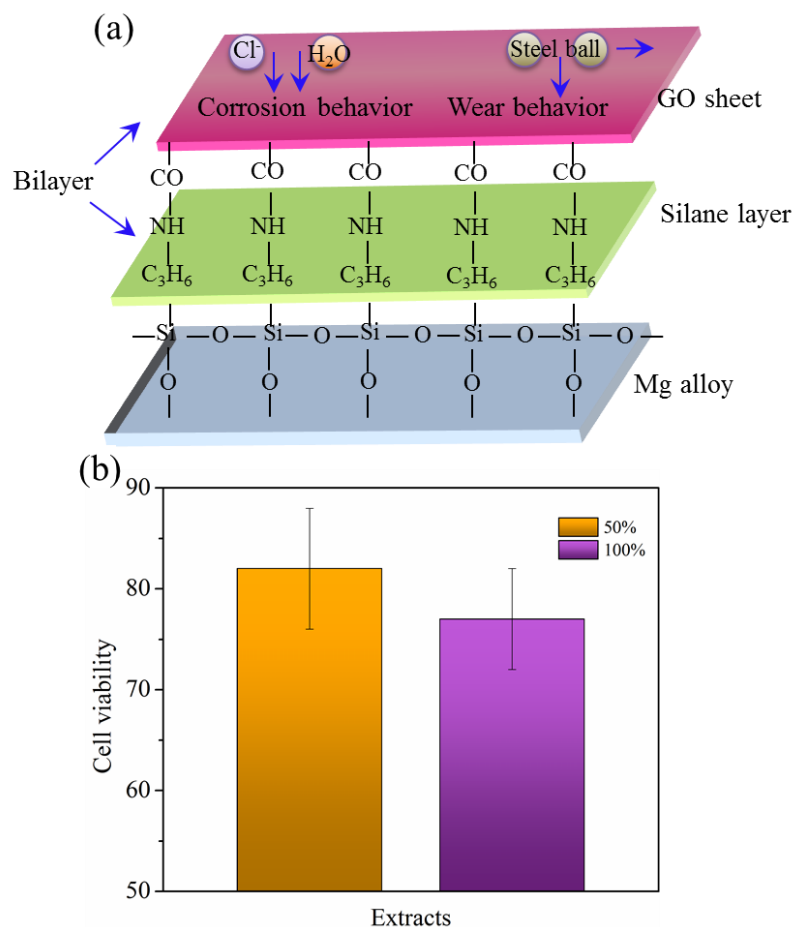
Figure 8. (**a**). Schematic diagram of anti-corrosion and anti-wear mechanisms for AZ91SG, and (**b**) its cytocompatibility for potential biomedical applications by using MG-63 cells.

GO sheet was one of the thinnest materials and consisted of carbon atoms which were arranged tightly in a 2D hexagonal layered structure. Moreover, its large surface area allowed it to readily prevent the direct contact of rough surfaces, reducing wear and friction. In this study, GO were chemically bonded on the silane layer through amidation reaction. The silane/GO composite coatings fully covered AZ91 Mg alloy surface in Figure 8a, which enhanced the load-carrying capacity by the way of migration or micro plastic deformation [55,66,67], thereby releasing the stress of wear process.

To determine the cytocompatibility of AZ91SG for potential biomedical applications, MG-63 cells were grown and cultured in its extracts for 72 h and the results are shown in Figure 8b. The cell viabilities of both extracts (50% and 100%) were both higher than 75% which was a standard of good cytocompatibility. This showed that AZ91SG supported the growth of cells, suggesting acceptable biocompatibility. One possible explanation for this phenomenon was that the degradation process of AZ91SG was significantly slowed down, as proven by immersion tests, H_2 release measurements. Moreover, pH and Mg^{2+} ion released from AZ91SG were lower than those of AZ91 or AZ91S. It should be noted that Mg^{2+} ion was 8 mEq/L after 24 h of accumulation in the SBF, which was lower than the required daily dietary intake of at least 24 to 30 mEq [68]. Mg^{2+} ion is metabolized out of the body, leaving only a small amount in the serum [69,70]. It was reported that with the increase of Mg^{2+} ion in the serum, different symptoms began to appear. Patients begin to develop ECG changes with Mg^{2+} of 5–10 mEq/L. At 10 mEq/L, a loss of deep tendon reflexes and muscle weakness happened. At 15 mEq/L, there were signs of abnormal conductivity surface as SA/AV node block, etc., according to the related study [71,72]. Based on the study of layer-by-layer self-assembly process, the resulting AZ91SG might be effectively applied in many biomedical fields, such as urinary stent, vascular stent, artificial joints, etc.

4. Conclusions

Silane/GO composite coatings were successfully prepared on AZ91 Mg alloy by the way of layer-by-layer self-assembly. The coating surface became rougher with *Pa* and *PSa* increased to 19.1 and 20.2 nm, respectively. The siloxane network (Si–O–Si) and Si–O-Mg bonds with high-density deposited on AZ91 Mg alloy. The further incorporation of GO through amidation reaction increased another physical barrier against corrosion, which was demonstrated by immersion tests due to the good adhesion of silane and the increased penetrating pathway length of corrosive medium even after immersion in SBF for 72 h. AZ91SG showed a very slow release of Mg ion ranging from 0.12 mM/cm^2 (24 h) to 0.34 mM/cm^2 (72 h) and was less alkaline in comparison with AZ91. Moreover, AZ91SG also generated small amount of H_2 during immersion tests in SBF. The cell viability of AZ91SG was higher than 75%, suggesting acceptable biocompatibility. The layer-by-layer self-assembly might be considered as an effective method to enhance the corrosion resistance of current Mg alloys for biomedical applications.

Author Contributions: Writing—original draft preparation, formal analysis, editing, T.L.; methodology, software, validation, funding acquisition, S.R.; writing—review, supervision, project administration, S.L. All authors have read and agreed to the published version of the manuscript.

Institutional Review Board Statement: Not Applicable.

Informed Consent Statement: Not Applicable.

Data Availability Statement: Data is contained within the article.

Conflicts of Interest: The authors declare no conflict of interest.

References

1. Li, Z.; Gu, X.; Lou, S.; Zheng, Y. The development of binary Mg–Ca alloys for use as biodegradable materials within bone. *Biomaterials* **2008**, *29*, 1329–1344. [CrossRef]
2. Xiang, D.; Li, S.; Yi, L.H.; Liu, T.F.; Liu, J.; Yang, C.M.; Zhou, L.H. In Situ Formation of Intermetallic Compound Bonding by Laser Cladding Al_2O_3 to Enhance the Corrosion Resistance of AZ31 Magnesium Alloy. *Lasers Eng.* **2020**, *45*, 309–323.
3. Li, S.; Yi, L.; Liu, T.; Ji, B.; Yang, C.; Zhou, L. Al_2O_3 eliminating defects in the Al coating by laser cladding to improve corrosion and wear resistance of Mg alloy. *Mater. Corros.* **2019**, *71*, 980–991. [CrossRef]
4. Özarslan, S.; Şevik, H.; Sorar, İ. Microstructure, mechanical and corrosion properties of novel Mg-Sn-Ce alloys produced by high pressure die casting. *Mater. Sci. Eng. C* **2019**, *105*, 1100641–1100648. [CrossRef]
5. Liu, J.; Bian, D.; Zheng, Y.; Chu, X.; Lin, Y.; Wang, M.; Lin, Z.; Li, M.; Zhang, Y.; Guan, S. Comparative in v itro study on binary Mg-RE (Sc, Y, La, Ce, Pr, Nd, Sm, Eu, Gd, Tb, Dy, Ho, Er, Tm, Yb and Lu) alloy systems. *Acta Biomater.* **2020**, *102*, 508–528. [CrossRef]
6. El-Kamel, R.S.; Ghoneim, A.A.; Fekry, A.M. Electrochemical, biodegradation and cytotoxicity of graphene oxide nanoparticles/polythreonine as a novel nano-coating on AZ91E Mg alloy staple in gastrectomy surgery. *Mater. Sci. Eng. C* **2019**, *103*, 109780–109788. [CrossRef] [PubMed]
7. Elbashar, Y. Surface Treatment of Aluminium 6061-T6 Using Multi-shot Laser Plasma Shock Processing (LPSP) Without Confinement. *Lasers Eng.* **2019**, *43*, 13–20.
8. Xia, D.; Liu, Y.; Wang, S.; Zeng, R.-C.; Liu, Y.; Zheng, Y.; Zhou, Y. In vitro and in vivo investigation on biodegradable Mg-Li-Ca alloys for bone implant application. *Sci. China Mater.* **2018**, *62*, 256–272. [CrossRef]
9. Li, J.N.; Shi, C.W.; Wang, Z.; Zhang, B.-L. Surface Modification of a Titanium Alloy with a Fe_3Al/Ti_3Al Matrix Laser Clad Composite Coating. *Lasers Eng.* **2019**, *43*, 35–46.
10. Singh, C.; Tiwari, S.; Singh, R. Exploring environment friendly nickel electrodeposition on AZ91 magnesium alloy: Effect of prior surface treatments and temperature of the bath on corrosion behaviour. *Corros. Sci.* **2019**, *151*, 1–19. [CrossRef]
11. Wang, B.; Xu, D.; Sun, J.; Han, E.-H. Effect of grain structure on the stress corrosion cracking (SCC) behavior of an as-extruded Mg-Zn-Zr alloy. *Corros. Sci.* **2019**, *157*, 347–356. [CrossRef]
12. Li, Y.; Yan, J.; Zhou, W.; Xiong, P.; Wang, P.; Yuan, W.; Zheng, Y.; Cheng, Y. In vitro degradation and biocompatibility evaluation of typical biodegradable metals (Mg/Zn/Fe) for the application of tracheobronchial stenosis. *Bioact. Mater.* **2019**, *4*, 114–119. [CrossRef] [PubMed]
13. Kunjukunju, S.; Roy, A.; Ramanathan, M.; Lee, B.; Candiello, J.E.; Kumta, P.N. A layer-by-layer approach to natural poly-mer-derived bioactive coatings on magnesium alloys. *Acta Biomater.* **2013**, *9*, 8690–8703. [CrossRef]
14. Liu, Z.; Wu, X.; Liu, X.; Xie, H.; Li, J. Effects of Al content on the corrosion properties of Mg–4Y–xAl alloys. *Mater. Corros.* **2020**, *71*, 1216–1225. [CrossRef]
15. Soltan, A.; Dargusch, M.S.; Shi, Z.; Gerrard, D.; Al Shabibi, S.; Kuo, Y.; Atrens, A. Corrosion of Mg alloys EV31A, WE43B, and ZE41A in chloride- and sulfate-containing solutions saturated with magnesium hydroxide. *Mater. Corros.* **2020**, *71*, 956–979. [CrossRef]
16. Li, G.; Su, J.; Zhao, X.; Chen, S.; Wu, R.; Wang, G. Effects of the addition of Na_2SnO_3 to NaCl electrolytes on Mg-14Li-3Al-1Gd electrode electrochemical behavior. *Mater. Corros.* **2019**, *71*, 564–570. [CrossRef]
17. Kang, Y.; Du, B.; Li, Y.; Wang, B.; Sheng, L.; Shao, L.; Zheng, Y.; Xi, T. Optimizing mechanical property and cytocompatibility of the biodegradable Mg-Zn-Y-Nd alloy by hot extrusion and heat treatment. *J. Mater. Sci. Technol.* **2019**, *35*, 6–18. [CrossRef]
18. Agarwal, S.; Morshed, M.; Labour, M.-N.; Hoey, D.; Duffy, B.; Curtin, J.; Jaiswal, S. Enhanced corrosion protection and biocompatibility of a PLGA–silane coating on AZ31 Mg alloy for orthopaedic applications. *RSC Adv.* **2016**, *6*, 113871–113883. [CrossRef]
19. Qiang, Y.; Zhang, S.; Zhao, H.; Tan, B.; Wang, L. Enhanced anticorrosion performance of copper by novel N-doped carbon dots. *Corros. Sci.* **2019**, *161*, 108193. [CrossRef]
20. Qiang, Y.J.; Guo, L.; Lan, X.J. Fabrication of environmentally friendly Losartan potassium film for corrosion inhibition of mild steel in HCl medium. *Chem. Eng. J.* **2021**, *406*, 126863–126876. [CrossRef]
21. Ma, L.; Qiang, Y.J.; Zhao, W.J. Designing novel organic inhibitor loaded MgAl-LDHs nanocontainer for enhanced corrosion resistance. *Chem. Eng. J.* **2021**, *408*, 127367–127379. [CrossRef]
22. Thanigaivelan, R.; Arunachalam, R.; Nithish, A.; Venkatesh, S.; Naveenkumar, P.; Selvaganapathy, S.; Aravind, A.S. Optimi-zation of Laser and Electrochemical Process Parameters for Surface Modification of Hardness and Hydrophobicity on 316L Steel. *Lasers Eng.* **2020**, *45*, 69–84.
23. Tian, Y.; Zhang, Z.; Li, J.N.; Huo, Y.S.; Su, M.L. Surface Modification of TA7 Titanium Alloy With Laser Clad La_2O_3 Amorphous Coatings. *Lasers Eng.* **2019**, *44*, 331–339.
24. Shen, Z.; Zhao, M.; Bian, D.; Shen, D.; Zhou, X.; Liu, J.; Liu, Y.; Guo, H.; Zheng, Y. Predicting the degradation behavior of mag-nesium alloys with a diffusion-based theoretical model and in vitro corrosion testing. *J. Mater. Sci. Technol.* **2019**, *035*, 1393–1402. [CrossRef]
25. Yilbas, B.; Ali, H.; Karatas, C.; Al-Sharafi, A.; Abu-Dheir, N.; Al-Qahtani, H.; Khaled, M. Laser Surface Treatment of Stainless Steel and Environmental Dust Effects. *Lasers Eng.* **2020**, *45*, 243–263.

26. Sharma, P.; Pandey, P.M. Corrosion behaviour of the porous iron scaffold in simulated body fluid for biodegradable implant application. *Mater. Sci. Eng. C* **2019**, *99*, 838–852. [CrossRef]

27. Liu, L.; Yang, Q.; Huang, L.; Liu, X.; Liang, Y.; Cui, Z.; Yang, X.; Zhu, S.; Li, Z.; Zheng, Y.; et al. The effects of a phytic acid/calcium ion conversion coating on the corrosion behavior and osteoinductivity of a magnesium-strontium alloy. *Appl. Surf. Sci.* **2019**, *484*, 511–523. [CrossRef]

28. Chang, J.-K.; Lin, C.-S.; Cheng, W.-J.; Lo, I.-H.; Wang, W.-R. Oxidation resistant silane coating for hot-dip galvanized hot stamping steel. *Corros. Sci.* **2020**, *164*, 108307. [CrossRef]

29. Matsuda, T.; Kashi, K.B.; Fushimi, K.; Gelling, V.J. Corrosion protection of epoxy coating with pH sensitive microcapsules encapsulating cerium nitrate. *Corros. Sci.* **2019**, *148*, 188–197. [CrossRef]

30. Montemor, M.; Pinto, R.; Ferreira, M. Chemical composition and corrosion protection of silane films modified with CeO2 nanoparticles. *Electrochim. Acta* **2009**, *54*, 5179–5189. [CrossRef]

31. Frignani, A.; Zucchi, F.; Trabanelli, G.; Grassi, V. Protective action towards aluminium corrosion by silanes with a long al-iphatic chain. *Corros. Sci.* **2006**, *48*, 2258–2273. [CrossRef]

32. Motte, C.; Poelman, M.; Roobroeck, A.; Fedel, M.; Deflorian, F.; Olivier, M.-G. Improvement of corrosion protection offered to galvanized steel by incorporation of lanthanide modified nanoclays in silane layer. *Prog. Org. Coat.* **2012**, *74*, 326–333. [CrossRef]

33. Guo, Y.; Zhang, Z.; Cao, Z.; Wang, D. Wear behavior of hollow glass beads (HGB) reinforced nitrile butadiene rubber: Effects of silane coupling agent and filler content. *Mater. Today Commun.* **2019**, *19*, 366–373. [CrossRef]

34. Yuan, R.; Ju, P.; Wu, Y.; Ji, L.; Li, H.; Chen, L.; Zhou, H.; Chen, J. Silane-grafted graphene oxide improves wear and corrosion resistance of polyimide matrix: Molecular dynamics simulation and experimental analysis. *J. Mater. Sci.* **2019**, *54*, 11069–11083. [CrossRef]

35. Kinoshita, H.; Nishina, Y.; Alias, A.A.; Fujii, M. Tribological properties of monolayer graphene oxide sheets as water-based lubricant additives. *Carbon* **2014**, *66*, 720–723. [CrossRef]

36. Li, Y.; Wang, Q.; Wang, T.; Pan, G. Preparation and tribological properties of graphene oxide/nitrile rubber nanocomposites. *J. Mater. Sci.* **2011**, *47*, 730–738. [CrossRef]

37. Song, H.-J.; Jia, X.-H.; Li, N.; Yang, X.-F.; Tang, H. Synthesis of α-Fe$_2$O$_3$ nanorod/graphene oxide composites and their tribological properties. *J. Mater. Chem.* **2011**, *22*, 895–902. [CrossRef]

38. Guo, B.; Chen, W.; Yan, L. Preparation of Flexible, Highly Transparent, Cross-Linked Cellulose Thin Film with High Mechanical Strength and Low Coefficient of Thermal Expansion. *ACS Sustain. Chem. Eng.* **2013**, *1*, 1474–1479. [CrossRef]

39. Saud, S.N.; Bakhsheshi-Rad, H.; Yaghoubidoust, F.; Iqbal, N.; Hamzah, E.; Ooi, C.R. Corrosion and bioactivity performance of graphene oxide coating on TiNb shape memory alloys in simulated body fluid. *Mater. Sci. Eng. C* **2016**, *68*, 687–694. [CrossRef] [PubMed]

40. Raghupathy, Y.; Kamboj, A.; Rekha, M.; Rao, N.N.; Srivastava, C. Copper-graphene oxide composite coatings for corrosion protection of mild steel in 3.5% NaCl. *Thin Solid Film* **2017**, *636*, 107–115. [CrossRef]

41. Li, M.; Liu, Q.; Jia, Z.; Xu, X.; Cheng, Y.; Zheng, Y.; Xi, T.; Wei, S. Graphene oxide/hydroxyapatite composite coatings fabricated by electrophoretic nanotechnology for biological applications. *Carbon* **2014**, *67*, 185–197. [CrossRef]

42. Raza, M.A.; Rehman, Z.U.; Ghauri, F.A. Corrosion study of silane-functionalized graphene oxide coatings on copper. *Thin Solid Film* **2018**, *663*, 93–99. [CrossRef]

43. Wang, Y.; Gu, Z.; Liu, J.; Jiang, J.; Yuan, N.; Pu, J.; Ding, J. An organic/inorganic composite multi-layer coating to improve the corrosion resistance of AZ31B Mg alloy. *Surf. Coatings Technol.* **2019**, *360*, 276–284. [CrossRef]

44. Li, P.F.; Zhou, H.; Cheng, X. Investigation of a hydrothermal reduced graphene oxide nano coating on Ti substrate and its nano-tribological behavior. *Surf. Coatings Technol.* **2014**, *254*, 298–304. [CrossRef]

45. Qi, S.; Li, X.; Dong, H. Improving the macro-scale tribology of monolayer graphene oxide coating on stainless steel by a silane bonding layer. *Mater. Lett.* **2017**, *209*, 15–18. [CrossRef]

46. Chu, J.H.; Tong, L.B.; Jiang, Z.H. Effect of Graphene Oxide/Silane Self-assemble Coating on Corrosion and Wear Resistance of Mg Alloy. *Surf. Technol.* **2019**, *48*, 62–68.

47. Schmidt, J.C.; Astasov-Frauenhoffer, M.; Waltimo, T.; Walter, C.; Weiger, R. Efficacy of various side-to-side toothbrushes and impact of brushing parameters on noncontact biofilm removal in an interdental space model. *Clin. Oral Investig.* **2016**, *21*, 1565–1577. [CrossRef] [PubMed]

48. Kirkland, N.; Birbilis, N.; Staiger, M. Assessing the corrosion of biodegradable magnesium implants: A critical review of current methodologies and their limitations. *Acta Biomater.* **2012**, *8*, 925–936. [CrossRef] [PubMed]

49. Jiao, G.; He, X.; Li, X.; Qiu, J.; Xu, H.; Zhang, N.; Liu, S. Limitations of MTT and CCK-8 assay for evaluation of graphene cyto-toxicity. *Rsc Adv.* **2015**, *5*, 53240–53244. [CrossRef]

50. Ciofani, G.; Danti, S.; D'Alessandro, D.; Moscato, S.; Menciassi, A. Assessing cytotoxicity of boron nitride nanotubes: Inter-ference with the MTT assay. *Biochem. Biophys. Res. Commun.* **2010**, *394*, 405–411. [CrossRef] [PubMed]

51. Souza, B.D.M.; Alves, A.M.H.; Ribeiro, D.M.; Santos, L.G.P.; Simões, C.M.O.; Felippe, W.T.; Felippe, M.C.S. Effect of milk renewal on cell viability in vitro at different time frames. *Braz. Dent. J.* **2017**, *28*, 435–439. [CrossRef]

52. Liu, X.; Yue, Z.; Romeo, T.; Weber, J.K.R.; Scheuermann, T.; Moulton, S.E.; Wallace, G.G. Biofunctionalized anti-corrosive silane coatings for magnesium alloys. *Acta Biomater.* **2013**, *9*, 8671–8677. [CrossRef] [PubMed]

53. Wang, H.R.; Wang, X.; Zhao, X.Y. Preparation and characterization of graphene oxide modified by silane coupling agent. *Appl. Chem. Ind.* **2019**, *48*, 97–100.

54. Wojciechowski, J.; Szubert, K.; Peipmann, R.; Fritz, M.; Schmidt, U.; Bund, A.; Lota, G. Anti-corrosive properties of silane coatings deposited on anodised aluminium. *Electrochimica Acta* **2016**, *220*, 1–10. [CrossRef]

55. Tong, L.; Zhang, J.; Xu, C.; Wang, X.; Song, S.; Jiang, Z.; Kamado, S.; Cheng, L.; Zhang, H. Enhanced corrosion and wear resistances by graphene oxide coating on the surface of Mg-Zn-Ca alloy. *Carbon* **2016**, *109*, 340–351. [CrossRef]

56. Zhou, M.; Zhou, Y.; Song, Q. ChemInform Abstract: Cu/Fe-Cocatalyzed Formation of β-Ketophosphonates by a Domino Knoevenagel-Decarboxylation-Oxyphosphorylation Sequence from Aromatic Aldehydes and H-Phosphonates. *Chemin-* **2015**, *46*. [CrossRef]

57. Lei, L.; Shi, J.; Wang, X.; Liu, D.; Xu, H. Microstructure and electrochemical behavior of cerium conversion coating modified with silane agent on magnesium substrates. *Appl. Surf. Sci.* **2016**, *376*, 161–171. [CrossRef]

58. Lu, X.; Zuo, Y.; Zhao, X.; Tang, Y. The improved performance of a Mg-rich epoxy coating on AZ91D magnesium alloy by silane pretreatment. *Corros. Sci.* **2012**, *60*, 165–172. [CrossRef]

59. Xue, B.; Yu, M.; Liu, J.; Li, S.; Xiong, L.; Kong, X. Corrosion Protective Properties of Silane Functionalized Graphene Oxide Film on AA2024-T3 Aluminum Alloy. *J. Electrochem. Soc.* **2016**, *163*, C798–C806. [CrossRef]

60. Zhang, D.F.; Fan, L.Z.; Guo, R.H.; Fan, Z.T. Preparation of FGO/PBMA Composites with Improved Thermal Stability. *Chem. J. Chin. Univ.* **2014**, *35*, 2466–2471.

61. Liu, Y.-C.; Liu, D.-B.; Zhao, Y.; Chen, M.-F. Corrosion degradation behavior of Mg–Ca alloy with high Ca content in SBF. *Trans. Nonferrous Met. Soc. China* **2015**, *25*, 3339–3347. [CrossRef]

62. Frutos, G. Local Surface Environment and Degradation Processes of Degradable Magnesium Biomaterials under Simulated Physiological Conditions. Ph.D. Thesis, University of Kiel, Kiel, Germany, 27 April 2020.

63. Gu, X.; Zheng, W.; Cheng, Y.; Zheng, Y. A study on alkaline heat treated Mg—Ca alloy for the control of the biocorrosion rate. *Acta Biomater.* **2009**, *5*, 2790–2799. [CrossRef]

64. Zhong, H.; Dai, L.; Yue, Y.; Zhang, B.; Feng, Z.; Zhang, X.; Ma, M.; Khosla, T.; Xiao, J.; Liu, R. Friction and wear behavior of an-nealed Ti-20Zr-6.5 Al-4V alloy sliding against 440 °C steel in vacuum. *Tribol. Int.* **2017**, *109*, 571–577. [CrossRef]

65. Richard, S.; SelwinRajadurai, J.; Manikandan, V.; Thanu, M.C.; Arumugaprabu, V.; Johnson, R.D.J. Study of tribological prop-erties of nano-sized red mud particle-reinforced polyester composites. *Trans. Indian Inst. Met.* **2019**, *72*, 2417–2431. [CrossRef]

66. Du, B.; Hu, Z.; Wang, J.; Sheng, L.; Zhao, H.; Zheng, Y.; Xi, T. Effect of extrusion process on the mechanical and in vitro degradation performance of a biomedical Mg-Zn-Y-Nd alloy. *Bioact. Mater.* **2020**, *5*, 219–227. [CrossRef] [PubMed]

67. Liu, S.; Kent, D.; Doan, N.; Dargusch, M.; Wang, G. Effects of deformation twinning on the mechanical properties of biode-gradable Zn-Mg alloys. *Bioact. Mater.* **2019**, *4*, 8–16. [CrossRef] [PubMed]

68. Ranade, V.V.; Somberg, J.C. Bioavailability and Pharmacokinetics of Magnesium After Administration of Magnesium Salts to Humans. *Am. J. Ther.* **2001**, *8*, 345–357. [CrossRef]

69. Sun, Z.L.; Wataha, J.C.; Hanks, C.T. Effects of metal ions on osteoblast-like cell metabolism and differentiation. *J. Biomed. Mater. Res.* **1997**, *34*, 29–37. [CrossRef]

70. Danscher, G.; Stoltenberg, M. Silver enhancement of quantum dots resulting from (1) metabolism of toxic metals in animals and humans, (2) in vivo, in vitro and immersion created zinc–sulphur/zinc–selenium nanocrystals, (3) metal ions liberated from metal implants and particles. *Prog. Histochem. Cytochem.* **2006**, *41*, 57–139. [CrossRef]

71. Krendel, D. Hypermagnesemia and Neuromuscular Transmission. *Semin. Neurol.* **1990**, *10*, 42–45. [CrossRef] [PubMed]

72. Turner, J.A. Diagnosis and management of pre-eclampsia: An update. *Int. J. Women's Health* **2010**, *2*, 327–337. [CrossRef] [PubMed]